Discharge mechanism of the heat treated electrolytic manganese dioxide cathode in a primary Li/MnO₂ battery: An in-situ and ex-situ synchrotron X-ray diffraction study

Wesley M. Dose [a], Neeraj Sharma [b], Scott W. Donne [a],*

[a] Discipline of Chemistry, University of Newcastle, Callaghan, NSW 2308, Australia
[b] School of Chemistry, University of New South Wales, Sydney, NSW 2052, Australia

HIGHLIGHTS

- The primary discharge mechanism of heat treated MnO₂ has been examined.
- In-situ and ex-situ synchrotron X-ray diffraction probed the structural evolution.
- Discharge was initially via simultaneous two-phase and solid solution reactions.
- Lithium is intercalated by a solid solution mechanism into the lithiated phase formed.

GRAPHICAL ABSTRACT
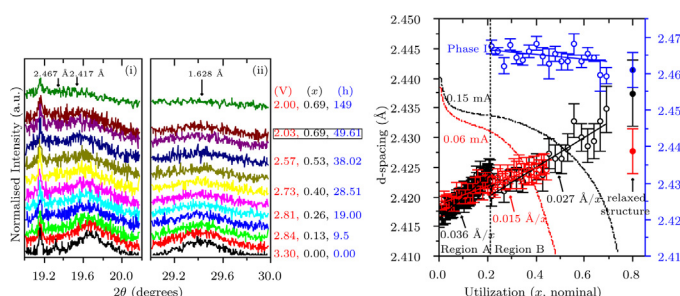
ARTICLE INFO

ABSTRACT

In this work the discharge mechanism for heat treated electrolytic manganese dioxide (HT-EMD) in a primary lithium battery is investigated. In-situ and ex-situ synchrotron X-ray diffraction is utilized to study the structural evolution with respect to material utilization (Li$_x$MnO₂). At a 4.3 mA g^{-1} discharge rate, HT-EMD undergoes a simultaneous two-phase transformation and solid solution reaction for $0 < x \lesssim 0.21$. Beyond this point both these processes continue in conjunction with a solid solution reaction of the lithiated phase (observed for $x > 0.34$) formed in the two phase process. At higher discharge rates (17.1 mA g^{-1}), no evidence for the new lithiated phase is observed, suggesting the discharge mechanism is rate dependent. These findings represent a key step in understanding the mechanistic behaviour of HT-EMD in primary battery systems, which in turn will assist in optimizing battery performance characteristics and broadening possible electronic applications.

1. Introduction

High resolution in-situ synchrotron X-ray diffraction (XRD) investigations using an electrochemical cell provide a unique means of following in real-time the crystal structure evolution of electrode materials during cell operation. This method has been used extensively to probe materials for Li-ion batteries [1–4] to assist in relating the electrode structure to electrochemical performance, and also to aid the search for new, better performing, electrode candidates. However, this technique has seldom been applied to the structural investigation of electrodes for primary battery systems. Lithium primary batteries are of particular importance, since they are often used to power long-life, critical devices, such as implantable pacemakers/defibrillators and other implantable

* Corresponding author. Tel.: +61 2 4921 5477; fax: +61 2 4921 5472..
  E-mail address: scott.donne@newcastle.edu.au (S.W. Donne).

medical electronic devices. Understanding the behaviour of primary battery systems is a fundamental step in optimizing their performance and broadening their applications.

The most common cathode material for non-aqueous lithium primary batteries is heat-treated electrolytic manganese dioxide (HT-EMD). The structure of the EMD precursor is traditionally described as a random intergrowth of the pyrolusite and ramsdellite manganese dioxide phases, which is progressively converted towards a pyrolusite-like structure with heat treatment [5–7]. The discharge mechanism for HT-EMD in Li/MnO$_2$ cells has been the focus of a number of investigations [6,8,9], although numerous differences can be noted between these proposed mechanisms.

Ohzuku et al. [6] performed an ex-situ X-ray diffraction (XRD) study on a series of partially reduced HT-EMD samples obtained electrochemically. Based on the diffraction patterns, these authors conclude that in the first half of reduction a two phase reaction was apparent that transforms the original material to a lithium inserted material with an expanded tetragonal unit cell. Following this was a homogenous process as lithium is inserted into an expanded tetragonal structure, occurring in the 30–90% stage of reduction. The final discharge product was fitted with an orthorhombic unit cell (consisting of two tetragonal sub-lattices).

In a later study, Shao-Horn et al. [8] investigated the $x = 0.1$ and 0.3 Li$_x$MnO$_2$ discharge products of a HT-EMD using ex-situ XRD and convergent beam electron diffraction (CBED). The CBED results indicated there were two processes in the discharge mechanism, the first being consistent with the first process in the work of Ohzuku et al. [6]. However, CBED analysis of the Li$_{0.3}$MnO$_2$ material was found to be incompatible with the orthorhombic super cell proposed as the final discharge product ($x = 0.88$) by Ohzuku et al. [6]. Hence, these authors proposed a different phase was formed during discharge, by a topotactic phase transformation, having a tetragonal unit cell consistent with the intermediate phase proposed by David et al. [10]. However, what structural changes this phase subsequently undergoes as lithium insertion continues beyond $x = 0.3$ to the full theoretical capacity of $x = 1.0$ is not considered by Shao-Horn et al. [8]. This therefore, may not dismiss the orthorhombic end-member structure proposed by Ohzuku et al. [6] as the final discharge product.

Most recently, Bowden et al. [9] employed a wide range of experimental techniques in their investigation of the discharge mechanism of HT-EMD, but drew mainly upon stepped potential electrochemical spectroscopy (SPECS), XRD and solid state magic angle spinning (MAS) NMR data. As in the mechanisms proposed by Ohzuku et al. [6] and Shao-Horn et al. [8], two main discharge processes were proposed, but these authors add a minor initial homogenous lithiation of the residual ramsdellite domains (∼2–3% of discharge). In contrast to the previous mechanisms, similarities between the ^{6}Li NMR spectra of partially lithiated HT-EMD and

ramsdellite led Bowden et al. [9] to propose that the first heterogenous process involved the lithiation of the defect pyrolusite structure, which resulted in the formation of an intermediate ramsdellite-like (orthorhombic unit cell) species in the first half of the discharge. The (apparent) presence of a transitory peak at 38° 2θ (CuKα) in the XRD pattern was claimed as support for this intermediate structure. Homogenous lithiation of the ramsdellite-like species then followed in the final process. Hence, the key difference between the mechanism of Bowden et al. [9] and Ohzuku et al. [6] is, perhaps, the stage at which an orthorhombic unit cell is called upon to fit the lithiated discharge products.

In summary, there exists considerable scope and necessity for further investigation of the changes to the crystal structure as lithium is intercalated into HT-EMD to reach a consensus on the proposed discharge mechanism. The objective of this work is to examine the crystal structure during discharge using both in-situ and ex-situ synchrotron X-ray diffraction in order to clarify the discrepancies in the literature relating to the discharge mechanism. Our in-situ synchrotron XRD technique provides high resolution and time-resolved information for the electrode behaviour in a real-cell environment. The discharge rate dependence of the crystal structure evolution will also be considered. Further, ex-situ methods (designed to avoid exposure of the air-sensitive partially reduced materials to the atmosphere) are employed, providing information on the relaxed electrode structure at various points in the discharge, without interference from various other battery components. This study represents, to our knowledge, the first comprehensive investigation of a primary lithium cathode material using in-situ synchrotron X-ray diffraction.

2. Experimental

EMD was prepared via anodic electrolysis onto two titanium electrodes, each 144 cm^2, submerged in a deposition bath with 0.1 M MnSO$_4$ and 0.25 M H$_2$SO$_4$ at 97 °C, and with an applied anodic current density of 65 A m^{-2}. The deposited material was mechanically removed from the electrode, washed thoroughly and then milled to a powder and sieved to give a powder with a mean particle size of 12.98 μm, and the particle size distribution as shown in Fig. 1. Additionally, an SEM image showing the morphological characteristics of the HT-EMD particles is also shown in Fig. 1.

Heat treatment parameters were determined using kinetic analysis, based on thermogravimetric experiments, reported previously [11]. Essentially, this identified the optimum thermal synthesis conditions by monitoring the progress of the reaction, in this case water loss from the surface and structure of EMD. Heat treatment was carried out by heating ∼10 g of EMD in a MTI GSL1300X tube furnace at 350 °C for 1.52 h in air, the parameters previously determined to be optimal for this material [12].
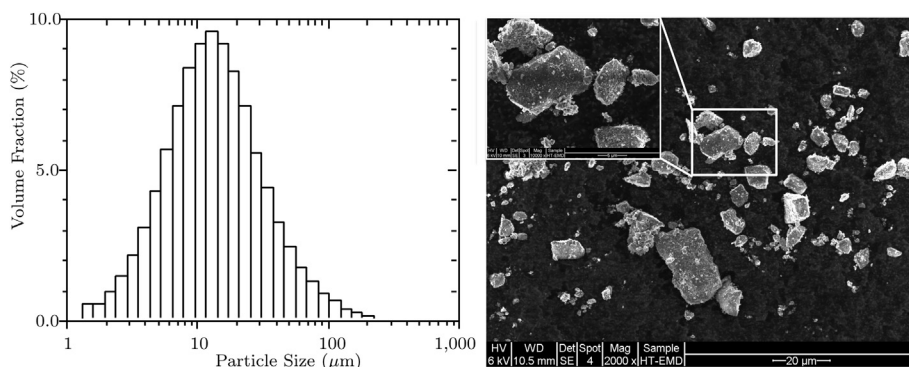

Fig. 1. Particle size distribution and SEM image of HT-EMD.

The properties of the HT-EMD were characterized by XRD (Panalytical X'Pert Pro MPD) to determine structure, N_2 gas adsorption to determine Brunauer–Emmett–Teller (BET) surface area and porosity, scanning electron microscopy (SEM, Phillips XL30) to determine morphology, and potentiometric titration to determine chemical composition [13].

Electrochemical testing was carried out using a Perkin Elmer VMP2 multi-channel potentiostat. CR2032 coin-type cells were assembled in an argon-filled glove box. The cathode was fabricated by first preparing a slurry of intimately mixed active material (75%), conductive carbon black (10%, Murablack India Ltd.) and poly-vinylidenedifluoride (15%, PVdF; binder, Fluka) in N-methyl-2-pyrrolidinone (NMP; Sigma–Aldrich). This was subsequently cast as a film (with thickness of 200 μm) onto electrochemical grade aluminium foil (20 μm thickness, Goodfellow) using an automatic film applicator (AFA-II, Shanghai Pushen Chemical Machinary Co. Ltd.) and allowed to dry in air. Punched electrodes (15 mm diameter) were then dried at 110 °C under vacuum prior to transferring them to the glove box for cell construction. The resulting electrode contained 3.5 ± 0.2 mg of active material. Lithium foil with a copper foil current collector (20 μm thickness, Goodfellow) served as the anode, while a Celgard 2400 sheet soaked in the electrolyte solution, 1 M $LiPF_6$ in 1:1 w/w ethylene carbonate/dimethyl carbonate, was employed as a separator.

In-situ synchrotron X-ray diffraction experiments were carried out in transmission mode on the powder diffraction beamline at the Australian Synchrotron [14,15]. The battery was a modified CR2032 coin-type cell [16]. The cells were constructed as before, although the stainless steel casings had 3 mm diameter holes drilled in their centre which were sealed with Kapton tape. Synchrotron X-ray diffraction data was collected in transmission geometry with the cell mounted in a similar fashion to that reported previously [15]. Data were collected continuously at 11 min per acquisition with a wavelength of 0.8262(1) Å, determined using the NIST660a LaB_6 standard reference material. The discharge currents tested were 0.015 mA (4.3 mA g^{-1}) and 0.060 mA (17.1 mA g^{-1}) during the collection of in-situ X-ray diffraction data for the primary discharge of the cell.

Ex-situ synchrotron X-ray diffraction data were collected on samples at various stages during the primary discharge, prepared by discharging cells at 0.040 mA (11.4 mA g^{-1}) to the desired composition before returning them to the glove box and disassembling the cell. The cathode was thoroughly washed with dimethyl carbonate and allowed to dry before being scraped off the aluminium substrate and sealed in a 0.3 mm diameter thin-walled (0.01 mm) boron-rich glass capillary (Charles Supper Company). Synchrotron X-ray diffraction data were collected using a wavelength of 0.8262(1) Å, determined using the NIST660a LaB_6 standard reference material, and data were collected for 11 min at ambient temperature using Debye–Scherrer geometry. The advantages of the ex-situ method are no contribution to the diffraction pattern from the in-situ cell components (including aluminium and copper foils, lithium metal, separator paper and electrolyte), and a higher mass of sample in the beam. In contrast to the in-situ data, however, the ex-situ materials have equilibrated to their metastable state.

Analysis of the in-situ data was performed using single peak fitting regimes in GSAS [17,18] and LAMP [19].

3. Results and discussion

3.1. Material physiochemical and electrochemical properties

The properties of HT-EMD are dependent on the synthesis conditions of the precursor EMD and the applied heating regime. It

Table 1
Properties of EMD and HT-EMD.

	Synthesis		P_r[b]	UCV ($Å^3$)[c]	Mn(IV) (%)	Mn(III) (%)	CVF[d]	H_2O (%)[e]	BET SA (m^2 g^{-1})[f]
	T (°C)[a]	Time (h)							
EMD	25	–	0.34	120.94	55.34	4.11	0.081	4.11	37.2
HT-EMD	350	1.52	0.83	115.34	54.94	6.00	0.00	0.84	24.9

[a] Heating temperature used for thermal synthesis.
[b] P_r: Pyrolusite fraction.
[c] UCV: Unit cell volume.
[d] CVF: Cation vacancy fraction.
[e] H_2O: Structural water removed >110 °C [13].
[f] BET SA: BET surface area.

is important therefore to characterize in detail the structure, morphology and chemical composition of the starting EMD and HT-EMD material, which have been summarized in Table 1. The electrochemical profile, differential capacity plot (dx/dE), specific capacity and material utilization of HT-EMD in an un-modified coin-type cell is shown in Fig. 2. The potential and differential capacity profiles demonstrate that for the majority of the discharge the potential is dropping (where dx/dE is close to zero), however this is preceded by a short region where the potential is flat/slightly increasing (indicated by large ± values for dx/dE) at ~2.8 V (as indicated by the arrow).

3.2. In-situ synchrotron X-ray diffraction

Fig. 3 shows a sample of the in-situ synchrotron XRD patterns for the cells discharged at 0.015 mA and 0.060 mA in the regions, $19.0° \leq 2\theta \leq 20.2°$ (2.50 Å $\leq d \leq 2.36$ Å) and $29.0° \leq 2\theta \leq 30.0°$ (1.65 Å $\leq d \leq 1.60$ Å), where the structural evolution for HT-EMD during discharge can be observed. The utilization and current-dependent change in the structural parameters for peaks in these regions are shown in Figs. 3 and 4, along with the in-situ electrochemical cell discharge profiles.

Early in the 0.015 mA discharge, both the 2.417 Å and 1.628 Å HT-EMD peaks lose intensity (Figs. 3b and 4b) without significant broadening of these reflections (Fig. 3c, d, 4c and d). The 2.417 Å
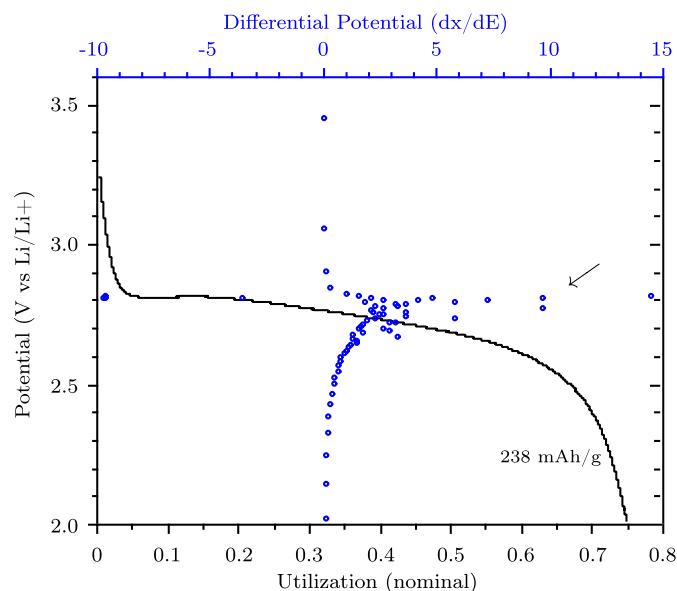
Fig. 2. Discharge curve and differential potential profile for HT-EMD in an unmodified cell.
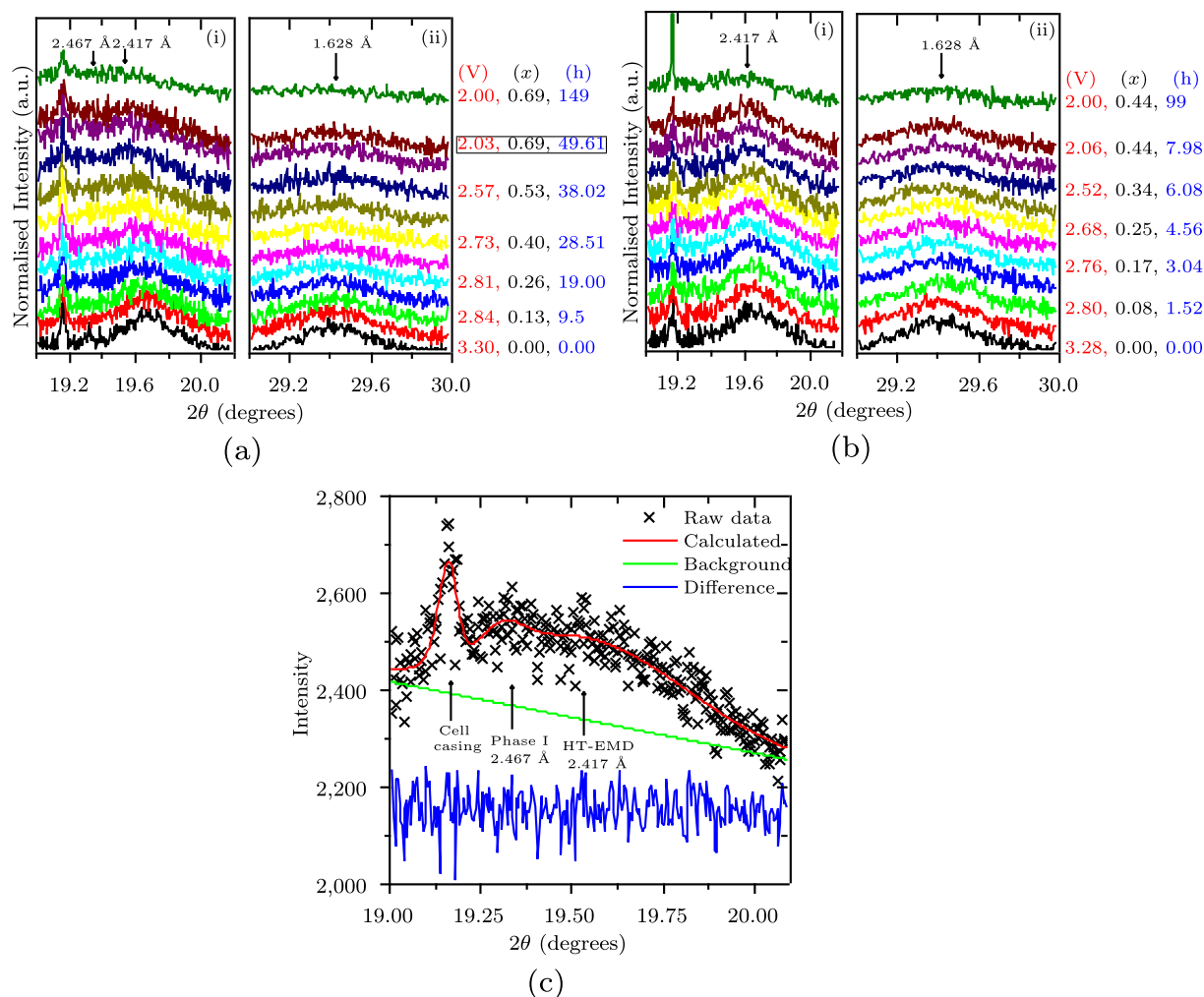
Fig. 3. In-situ X-ray diffraction patterns for HT-EMD discharged at (a) 0.015 mA, and (b) 0.060 mA. The potential (V), state of discharge (x), and time (h) of each spectrum is labelled. Patterns acquired at open circuit potential prior to (bottom), and 6 days after (top), discharging the cell are also shown. More than 250 patterns were collected during the discharge; here, every 25th pattern is shown, and only a limited 2θ range, (i) $19.0 \le 2\theta \le 20.2°$ and (ii) $29.0 \le 2\theta \le 30.0°$, of each pattern is shown. (c) Example of peak-fitting profiles and the corresponding difference plot, applied to the 0.015 mA spectrum indicated by the box in (a), where both HT-EMD and Phase I are present.

peak is seen to move to larger d-spacings (Fig. 4a), although the 1.628 Å peak does not shift (Fig. 5a). This suggests that the expansion of the lattice is non-uniform, with greater expansion in some crystallographic planes than in others. Beyond $x = 0.21$ a new peak appears, and could be fitted (see Fig. 3c), at 2.467 Å, close by the 2.417 Å HT-EMD peak. Based on the ex-situ synchrotron data (discussed later), the new peak represents the formation of a new phase, which we denote Phase I. This necessitated a two-peak fitting regime in this 2θ range, and hence the 0.015 mA discharge is divided into two regions: Region A, where only peaks characteristic of HT-EMD are present, and Region B, in which there are peaks from HT-EMD and Phase I. The 2.467 Å peak from Phase I, the lithiated HT-EMD phase, was also observed in the ex-situ XRD study by Ohzuku et al. [6] and Bowden et al. [9]. This work reveals the point in the discharge where the new phase is first observed, and also provides details of the progressive changes in this phase with ongoing lithiation.

The peak ratio (Fig. 4b, taken as the ratio of the phase fraction of the peak from Phase I and that for the neighbouring peak from the cell casing (internal reference)) and GW (Fig. 4c, a GSAS parameter extracted from the peak profile function, and directly proportional to the Gaussian variance of the peak [20,21]) of Phase I increase

rapidly at first, and then more slowly, as Li⁺ intercalation proceeds, indicating this phase is becoming more prominent. The increase in Phase I occurs at the expense of the HT-EMD, as indicated by the gradual decrease in peak height of the 2.417 Å HT-EMD reflection (Fig. 4b). This begins in Region A, therefore preceding the emergence of the peaks corresponding to Phase I. The late emergence of the Phase I reflections could be in response to an internal stress in the newly formed Phase I, caused by the progressive movement of the phase boundary between the HT-EMD phase and Phase I with deeper discharge. This would induce a lattice disorder in the matrix, thereby delaying the appearance of the Phase I diffraction peaks until the internal stresses are relieved and the fraction of a well ordered phase increases [6].

In region B, the 2.417 Å HT-EMD peak continues to shift to higher d-spacing (Fig. 4a), indicating that this phase continues to accommodate Li⁺, while also becoming broader (increase in GW, Fig. 4c), especially towards the latter stages of cell life. Broadening is a feature of both the HT-EMD and Phase I peaks in Region B of the discharge. This loss of material crystallinity suggests the formation of lattice defects, in the form of microstrain and/or stacking faults, or cracking of the crystal particles into smaller ones as a result of the electrochemical process.
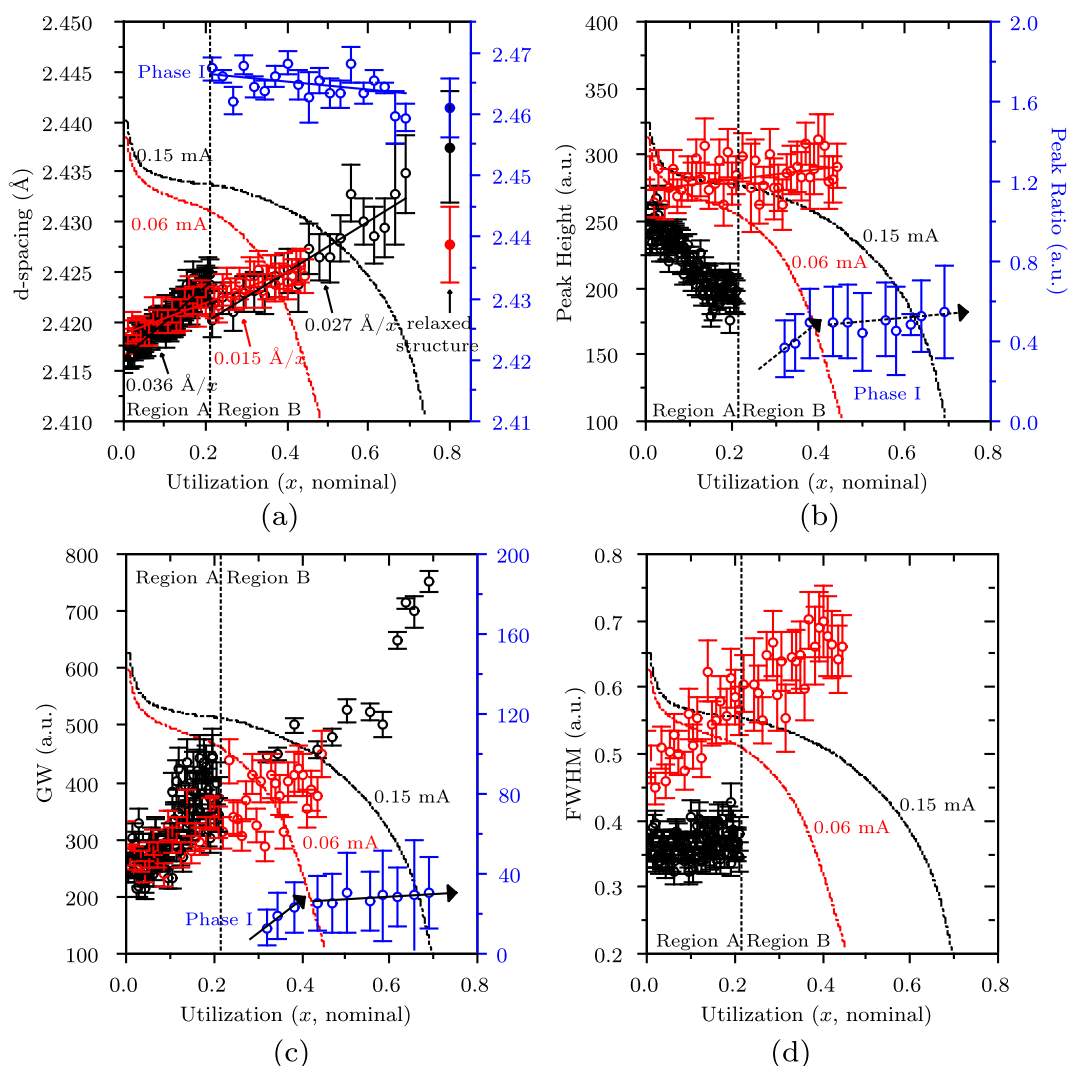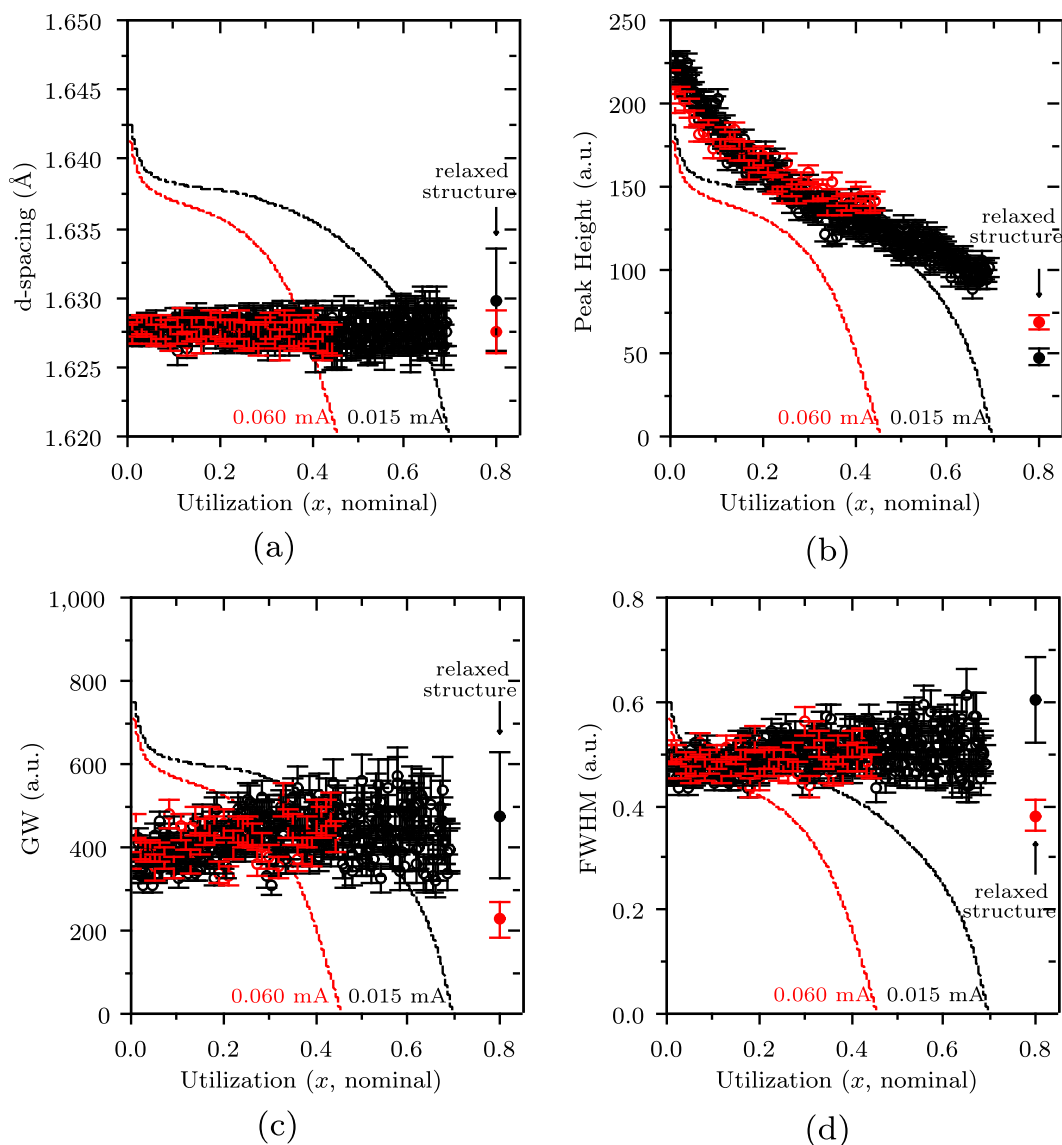
Fig. 4. The (a) d-spacing, (b) peak height and peak ratio (described in text), (c) GW (described in text), and (d) peak full width at half maximum (FWHM) for the 2.417 Å HT-EMD peak and Phase I as a function of MnO_2 utilization, shown against the discharge profile. The black (HT-EMD) and blue (Phase I) data are for the 0.015 mA discharge, while the red (HT-EMD) data is for the 0.060 mA discharge. For the 0.015 mA data, the discharge is split into two regions: Region A, where only the HT-EMD phase is present, and Region B, where the Phase I peak emerges close by the HT-EMD peak. The filled data points shown at $x = 0.80$ (arbitrary) represent the relaxed structure measured after 6 days for the 0.015 mA cell and 4 days for the 0.060 mA cell. (For interpretation of the references to colour in this figure legend, the reader is referred to the web version of this article.)

The data shows that throughout the discharge of HT-EMD the two-phase and solid-solution reactions occur concurrently. This is indicated by the simultaneous decrease in intensity of the 2.417 Å HT-EMD peak and the shifting of this peak to larger d-spacings. Other real-time, non-equilibrium mechanistic studies of battery cathode materials have also reported the simultaneous occurrence of two-phase and solid-solution reactions [22]. The behaviour of Phase 1 will be discussed with ex-situ data, as this provides superior resolution, especially considering that this reflection in in-situ data overlaps with a cell casing reflection.

In the 0.060 mA discharge, however, the Phase I peak is not observed in the diffraction patterns, suggesting the process via which it forms is current-dependent. To confirm that the formation of Phase I was not kinetically limited, and therefore not observed some time after the more rapid, higher current, 8.0 h discharge (compared to 49.6 h for the 0.015 mA cell), diffraction patterns for both the 0.015 mA and 0.060 mA batteries were taken 6 and 4 days, respectively, after the end of discharge. Diffraction patterns (Fig. 3) and peak structural parameters (Figs. 3 and 4,

filled data points at $x = 0.80$, arbitrary) for the 'relaxed structures' are shown. No new peaks were seen to emerge in the diffraction patterns of either cathode material after this time. The higher rate discharge also resulted in a significantly increased rate of peak broadening, and hence loss of crystallinity, for the 2.417 Å HT-EMD peak (Fig. 4c). This is likely due to the increased strain placed upon the expanded HT-EMD lattice, which, since no new phases are observed to form, must carry all the charge for the 0.060 mA discharge. Further, in contrast to the 0.015 mA electrode behaviour, the intensity of the 0.060 mA 2.417 Å reflection remains relatively constant (Fig. 4b), which is consistent with no new phases forming, including small crystallites. Surprisingly, despite lithium insertion occurring exclusively into the HT-EMD phase at the higher discharge rate, the rate of change in d-spacing (lattice expansion) of the 2.417 Å HT-EMD peak at 0.060 mA (0.015 Å/x) is less than that for the slower 0.015 mA discharge in both Region A (0.036 Å/x) and Region B (0.027 Å/x). The behaviour of the 1.628 Å HT-EMD peak shows virtually no current dependence (Fig. 5).

Fig. 5. The (a) d-spacing, (b) peak height, (c) GW, and (d) peak full width at half maximum (FWHM) for the 1.628 Å HT-EMD peak as a function of MnO_2 utilization, shown against the discharge profile. The black data is for the 0.015 mA discharge, while the red data is for the 0.060 mA discharge. The filled data points shown at $x = 0.80$ (arbitrary) represent the relaxed structure measured after 6 days for the 0.015 mA cell and 4 days for the 0.060 mA cell. (For interpretation of the references to colour in this figure legend, the reader is referred to the web version of this article.)
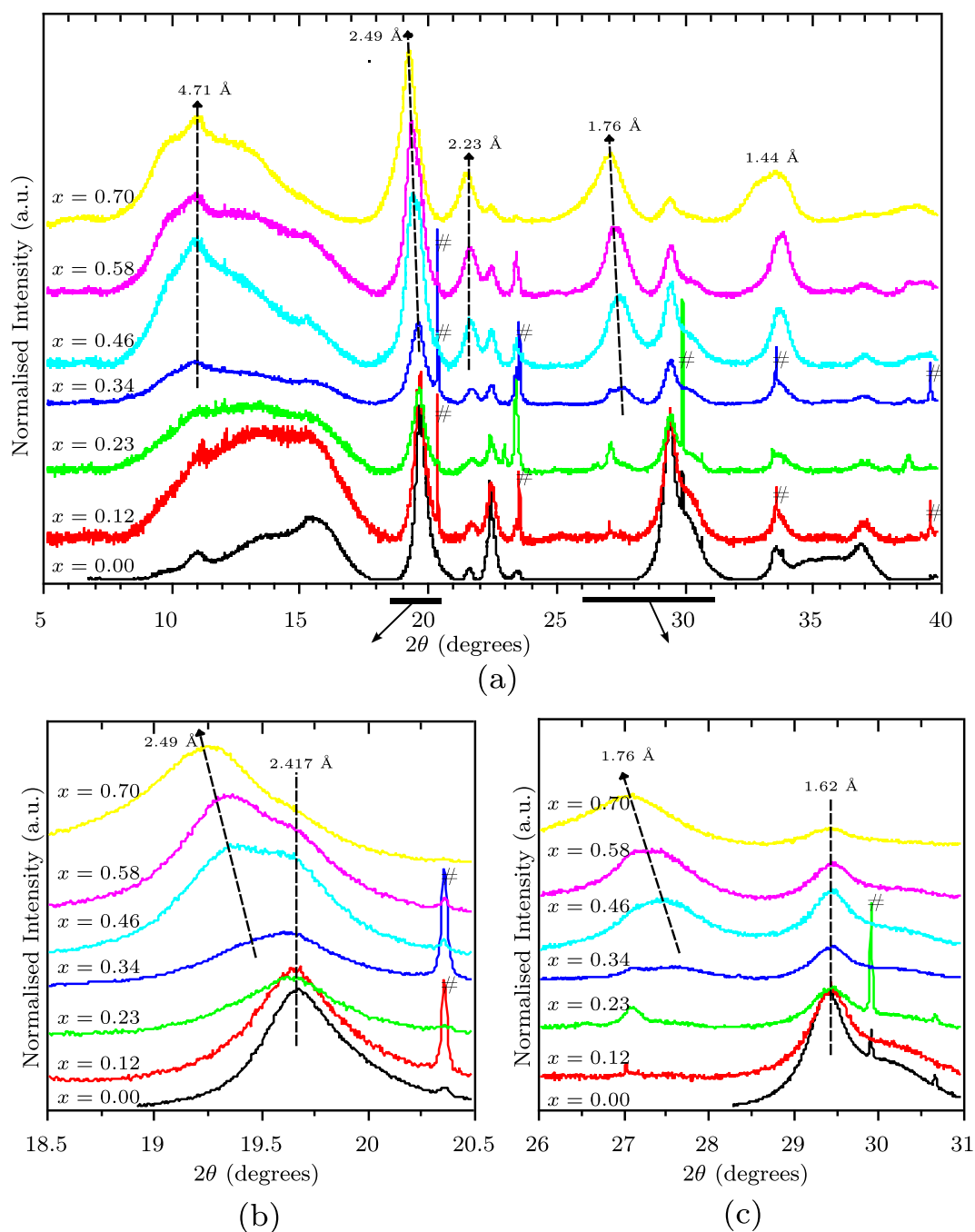
3.3. Ex-situ synchrotron X-ray diffraction

The ex-situ synchrotron XRD patterns of HT-EMD measured at progressive partial discharge states are shown in Fig. 6a. Sharp reflections due to traces of aluminium foil scraped off the cathode substrate when the cathode material was removed are marked with (#). Fig. 5b and c shows the structural changes with respect to lithiation degree in the regions $18.5° \leq 2\theta \leq 20.5°$ (2.57 Å $\leq d \leq 2.32$ Å) and $26° \leq 2\theta \leq 31°$ (1.84 Å $\leq d \leq 1.55$ Å) in more detail.

Comparing the trends in the in-situ (Figs. 3 and 4) and ex-situ (Fig. 6) data, we observe that the electrochemically reduced ex-situ materials show similar trends with degree of discharge to those reduced in real-time in a cell environment. For example, the peak at $19.68° 2\theta$ (2.417 Å) in the ex-situ data (Fig. 6b) corresponds to the HT-EMD reflection observed in the in-situ patterns at 2.417 Å (behaviour shown in Fig. 4). The ex-situ analysis shows this peak moves to lower 2θ angles (higher d-spacing) and broadens with

discharge (Fig. 6b). These trends are also observed in the in-situ data, as discussed previously. Further, for the ex-situ materials reduced with $x > 0.34$, a new peak is seen to emerge close by the $19.68° 2\theta$ (2.417 Å) HT-EMD peak at $19.39° 2\theta$ (2.453 Å) in the ex-situ data (Fig. 6b), which corresponds to the Phase I peak observed to emerge in the in-situ study at 2.467 Å for $x \gtrsim 0.21$. This indicates that the discharge rate of 0.040 mA used in the preparation of the ex-situ samples leads to a reduction mechanism similar to that observed for the 0.015 mA in-situ cell. However, it differs from the 0.060 mA in-situ cell since the 2.453 Å peak from Phase I is not observed at the higher rate discharge. Therefore, the ex-situ data collected provides additional detail that corroborate the low rate discharge behaviour of HT-EMD.

Considering now the ex-situ X-ray diffraction patterns as a whole (Fig. 6a), in the early part of discharge, i.e., $x < 0.34$, the $2\theta = 15.50, 19.68, 22.44$ and $29.49°$ peaks characteristic of HT-EMD decrease in intensity. This is highlighted in Fig. 5b and c for the $2\theta = 19.68$ and $29.49°$ peaks. No new peaks are seen to emerge in

Fig. 6. (a) Ex-situ synchrotron X-ray diffraction patterns of HT-EMD taken at various degrees of discharge at a 0.040 mA rate. (b) and (c) highlight the changes in the diffraction patterns in the regions $18.5 \leq 2\theta \leq 20.5°$ (2.57 Å $\leq d \leq$ 2.32 Å) and $26 \leq 2\theta \leq 31°$ (1.84 Å $\leq d \leq$ 1.55 Å), respectively. Peaks arising from Al foil scraped from the current collector with the removal of the cathode material are marked with (#).

the $x < 0.34$ patterns, which, in light of the better resolution afforded in the ex-situ measurements, further emphasizes this phase is not observed in the diffraction data until the internal stresses from the phase transition are relieved and the fraction of a well-ordered phase increases. The peak behaviour in this region is indicative of a two-phase system, which is consistent with the plateau at 2.8 V (vs. Li/Li$^+$) in this region of the discharge curve (Fig. 2). Direct evidence for the solid-solution reaction in this region is not observed in the ex-situ data due to the relatively small shifts in the position of the 2.417 Å HT-EMD peak (Fig. 4a), and it might be associated with a process that relaxes during the equilibration that occurs with ex-situ samples.

As lithiation progresses beyond $x > 0.34$, new reflections are observed at $2\theta = 10.20, 19.37, 21.64, 27.44$ and $33.74°$ (emerging peaks at $2\theta = 19.37$ and $27.44°$ are highlighted in Fig. 5b and c). These peaks are marked by (*) in Fig. 6a. This is indicative of the formation of a new phase, previously denoted Phase I. After emerging, these peaks shift to higher d-spacings (Fig. 5b and c), indicating lithium ions are inserted into the newly formed Phase I via a single phase mechanism, and thus the formation of a solid solution. Also in this region the $2\theta = 15.50, 19.68, 22.44$ and $29.49°$ HT-EMD peaks continue to decrease in intensity, suggesting lithium intercalation into the remaining HT-EMD and the associated phase transition to Phase I, is a continued mode of carrying charge.

Table 2
Comparison of lithiated HT-EMD diffraction data from Ohzuku et al. [6], Shao-Horn et al. [8], Bowden et al. [9] and this work.

	Ohzuku et al. [6]	Shao-Horn et al. [8]		Bowden et al. [9]	This work
	XRD	XRD	CBED	XRD	Synchrotron XRD
Unit cell (Å)	Orthorhombic super-lattice $a = 10.27$ $b = 4.93$ $c = 2.85$	Tetragonal $a = \sim 10$ $c = \sim 5.7$		Ramsdellite-like (orthorhombic) $a = 10.1$ $b = 2.9$ $c = 4.8$	
d-spacing (Å)	4.4–6	4.54–89			4.71
	3.5–6[a]		~ 3.5		
	2.45			2.49	2.49
				2.37[b]	
	2.20				2.23
	1.76	1.68–71	~ 1.7	1.79	1.76
	1.43				1.44

[a] Expected based on unit cell assignment, but not observed in XRD pattern.
[b] (Apparent) peak at 38° 2θ (CuKα) referred to in text of Bowden et al. [9], but not observed in other investigations.

Table 2 compares the d-spacing of the Phase I reflections at $x = 0.70$ with other literature values for the lithiated HT-EMD end of discharge structure. Despite the differences in the mechanisms and crystal structures proposed in previous reports, the peak position data shows good agreement. The ~ 3.5–3.6 Å peak expected (although not observed) in the model proposed Ohzuku et al. [6], and observed by Shao-Horn et al. [8] in their CBED analysis, was not observed in our synchrotron XRD study. However, our ex-situ diffraction patterns show broad features in this region ($\sim 13.5°$ 2θ), associated with the use of quartz capillaries, which may mask its presence. Further, the peak at ~ 2.37 Å used by Bowden et al. [9] as evidence for the formation of an intermediate ramsdellite-like phase was not observed in our investigation, nor is it seen in other proposed mechanisms [6,8].

The similarities in Table 2 indicate that the apparent differences between these investigations may, in part, be due to the broad features in the diffraction patterns of the discharged materials, meaning more than one crystal structure can be proposed. Subtle differences may also stem from the properties of the HT-EMD used, which in turn relies on the properties of the EMD. For example, the preparation conditions (temperature/time) used are; 400 °C for 7 days (Ohzuku et al. [6]), 375 °C for 12 h under flowing N$_2$ (Shao-Horn et al. [8]), unspecified (Bowden et al. [9]), and 350 °C for 1.52 h under static air in this work. Our previous work has found that the temperature, time and atmosphere all have significant bearing on the heat treated material physiochemical properties and electrochemical performance [12,23], and hence, may also influence the finer aspects of the discharge mechanism.

Therefore, this work has made the following contributions to the understanding of the discharge mechanism of HT-EMD:

i) The structural evolution, and therefore the discharge mechanism, of HT-EMD as lithium is intercalated is found to be dependent on the rate of discharge.

ii) The real-time data collected here provides clarification on the mechanism and at which stage the various reactions are occurring.

(a) For a 4.3 mA g^{-1} discharge rate, the discharge mechanism proceeds via simultaneous two-phase and solid-solution reactions. Throughout the discharge homogeneous lithium intercalation into HT-EMD and a heterogeneous phase change from the starting HT-EMD structure to Phase I are observed. At this low discharge rate, the kinetics of the chemical transformation process in forming Phase I are sufficiently fast such that the new phase is formed and is available for reduction via the two-phase mechanism. In addition, after Phase I forms, lithium is intercalated into this structure via a homogenous mechanism.

(b) At higher discharge rates (17.1 mA g^{-1}), where the kinetics of the chemical transformation to form the new phase are relatively slower, reduction was found to proceed in the solid solution throughout the course of discharge since no other phase was kinetically able to form.

iii) In-situ data collected in the early stages of the discharge did not show evidence for the initial minor process involving the lithiation of ramsdellite proposed by Bowden et al. [9]. The early homogeneous lithiation of HT-EMD may be related to what these authors observed, however further investigation is required. Collecting high resolution ex-situ diffraction patterns on an increased number of materials from the early stages of reduction may assist in verifying the existence of this step.

iv) The point in the discharge at which Phase I is observed in the diffraction patterns is found to be earlier than indicated in the literature [6,8,9]. The ex-situ synchrotron XRD data showed direct evidence of Phase I from $x > 0.34$, although in-situ data may indicate that lithium insertion into the newly formed lithiated phase starts as early as $x \gtrsim 0.21$.

v) Data collected in-situ, in a real cell environment, provides detailed information regarding the evolution of the crystal structure with respect to discharge. These findings are supported by the high resolution ex-situ data, which further highlight the changes to the HT-EMD and new lithiated phase.

4. Conclusions

In summary, this work investigated the dependence of the structural evolution of HT-EMD on discharge rate in a primary lithium battery. For a 4.3 mA g^{-1} discharge rate we find that in the region $0 < x \lesssim 0.21$ both solid-solution and two-phase reactions are occurring simultaneously within an HT-EMD cathode. This causes a non-uniform expansion of the crystal lattice but only slight losses in the material crystallinity and a progressive decrease in the HT-EMD phase fraction, although evidence for the new lithiated phase, denoted Phase I, is only observed for $x \gtrsim 0.21$. Beyond this point, both the solid-solution and two-phase discharge processes continue, evidenced by the shift in the 2.417 Å HT-EMD peak and the initially rapid and then more gradual increase in the intensity of peaks assigned to the new lithiated phase. This occurs at the expense of the HT-EMD phase, whose peaks continue to decrease in intensity. In addition to these two processes, in the region $x > 0.34$

(although possibly as early as $x \gtrsim 0.21$) the charge begins to be carried by the newly formed lithiated phase. The crystal structure of this newly formed phase has not been resolved because of the broad features in the diffraction patterns. Lithium ions are inserted into this phase via a homogenous mechanism, which causes an expansion of the crystal structure and a decrease in the material crystallinity. At higher discharge rates (17.1 mA g^{-1}) peaks from Phase I are not observed in the diffraction patterns, implying lithium is inserted into the HT-EMD phase via a solid-solution reaction for the entire discharge.

Acknowledgements

References

[1] X.Q. Yang, X. Sun, S.J. Lee, J. McBreen, S. Mukerjee, M.L. Daroux, X.K. Xing, Eletrochem. Solid State Lett. 2 (1999) 157–160.
[2] K.Y. Chung, W.-S. Yoon, J. McBreen, X.-Q. Yang, S.H. Oh, H.C. Shin, W.I. Cho, B.W. Cho, J. Power Sources 174 (2007) 619–623.
[3] H.-H. Chang, C.-C. Chang, H.-C. Wu, M.-H. Yang, H.-S. Sheu, N.-L. Wu, Electrochem. Commun. 10 (2008) 335–339.
[4] Y.-C. Chen, J.-M. Chen, C.-H. Hsu, J.-W. Yeh, H.C. Shih, Y.-S. Chang, H.-S. Sheu, J. Power Sources 189 (2009) 790–793.
[5] Y. Chabre, J. Pannetier, Prog. Solid State Chem. 23 (1995) 1–130.
[6] T. Ohzuku, M. Kitagawa, T. Hirai, J. Electrochem. Soc. 136 (1989) 3169–3174.
[7] W. Bowden, C.P. Grey, S. Hackney, F. Wang, Y. Paik, N. Iltchev, R. Sirotina, J. Power Sources 153 (2006) 265–273.
[8] Y. Shao-Horn, S.A. Hackney, B.C. Cornilsen, J. Electrochem. Soc. 144 (1997) 3147–3153.
[9] W. Bowden, C. Grey, S. Hackney, X.Q. Yang, Y. Paik, F. Wang, T. Richards, R. Sirotina, ITE Lett. Batter. New. Technol. Med. 3 (2002) 312–336.
[10] W.I.F. David, M.M. Thackeray, P.G. Bruce, J.B. Goodenough, Mater. Res. Bull. 19 (1984) 99–106.
[11] W.M. Dose, S.W. Donne, J. Therm. Anal. Calorim. 105 (2011a) 113–122.
[12] W.M. Dose, S.W. Donne, J. Electrochem. Soc. 158 (2011b) A905–A912.
[13] W.M. Dose, S.W. Donne, Mater. Sci. Eng. 176 (2011c) 1169–1177.
[14] K.S. Wallwork, B.J. Kennedy, D. Wang, in: AIP Conference Proceedings, vol. 879, 2007, pp. 879–882.
[15] W.R. Brant, S. Schmid, G. Du, Q. Gu, N. Sharma, J. Power Sources 244 (2013) 109–114.
[16] Y.-H. Kao, M. Tang, N. Meethong, J. Bai, W.C. Carter, Y.-M. Chiang, Chem. Mater. 22 (2010) 5845–5855.
[17] A. Larson, R. Von Dreele, Los Alamos National Laboratory Report LAUR, 1994, pp. 86–748.
[18] B.H. Toby, J. Appl. Crystallogr. 34 (2001) 210–213.
[19] D. Richard, M. Ferrand, G.J. Kearley, J. Neutron Res. 4 (1996) 33–39.
[20] G. Caglioti, A. Paoletti, F.P. Ricci, Nucl. Instrum. 3 (1958) 223.
[21] P.W. Stephens, J. Appl. Crystallogr. 32 (1999) 281–289.
[22] N. Sharma, X. Guo, G. Du, Z. Guo, J. Wang, Z. Wang, V.K. Peterson, J. Am. Chem. Soc. 134 (2012) 7867–7873.
[23] W.M. Dose, S.W. Donne, J. Power Sources 247 (2014) 852–857.